Electrochemical stability of $RuO_2(110)/Ru(0001)$ model electrodes in the oxygen and chlorine evolution reactions

Andrey Goryachev [a, 1, 2], Marco Etzi Coller Pascuzzi [a, 1], Francesco Carlà [b, 3], Tim Weber [c], Herbert Over [c, ***], Emiel J.M. Hensen [a, **], Jan P. Hofmann [a, *]

[a] Laboratory of Inorganic Materials and Catalysis, Department of Chemical Engineering and Chemistry, Eindhoven University of Technology, P.O. Box 513, 5600MB, Eindhoven, the Netherlands
[b] Beamline ID03, European Synchrotron Radiation Facility, 71 Avenue des Martyrs, 38000, Grenoble, France
[c] Physikalisch-Chemisches Institut, Justus-Liebig-Universität Giessen, Heinrich-Buff-Ring 17, 35392, Giessen, Germany

ARTICLE INFO

ABSTRACT

RuO_2 is commercially employed as an anodic catalyst in the chlor-alkali process. It is also one of the most active electrocatalysts for the oxidation of water, relevant to electrochemical water splitting. However, the use of RuO_2 is limited by its low anodic stability under acidic conditions, especially at high overpotentials. In the present work, the electrochemical stability of model $RuO_2(110)/Ru(0001)$ anodes was investigated in order to gain a deeper understanding of the relation between structure and performance in Cl_2 and O_2 evolution reactions (CER and OER, respectively). Online electrochemical mass spectrometry was used to determine the onset potential of CER and OER in HCl and H_2SO_4 electrolytes, respectively. The onset potential of OER was higher in HCl than in H_2SO_4 due to competition with the kinetically more favorable CER. A detailed stability evaluation revealed pitting corrosion of the electrode surface with exposure of Ru(0001) metal substrate concomitant with the formation of a hydrous RuO_2 in some areas regardless of the applied electrochemical treatment. However, despite local pitting, the $RuO_2(110)$ layer preserves its thickness in most areas. Degradation of the electrode was found to be less severe in 0.5 M HCl due to a decrease in the faradaic efficiency of RuO_2 oxidation caused by competition with the kinetically more favorable CER.

© 2020 Eindhoven University of Technology. Published by Elsevier Ltd. This is an open access article under the CC BY license (http://creativecommons.org/licenses/by/4.0/).

1. Introduction

RuO_2 is a common electrocatalyst which is primarily used for large-scale electrochemical production of Cl_2 as a part of mixed oxide anodes (Dimensionally Stable Anodes, DSA®) [1–4]. Nearly all chlorine is produced by electrolysis of concentrated NaCl solution (brine) in the chlor-alkali process with an annual global production of ca. 70 million tons of Cl_2 [5,6]. Chlorine is used as a base chemical for a wide range of applications including metallurgy, polymerization, and organic synthesis [7]. Besides the production of Cl_2, the chlor-alkali process yields NaOH and H_2 as by-products, which are typically used in oil refineries and in the manufacture of paper, soap, and textiles [8].

A major challenge with the use of RuO_2 is the competition of the desired anodic oxidation of Cl^- with the formation of gaseous oxygen as a result of water oxidation. Although the oxygen evolution reaction (OER) is thermodynamically favored over the CER in all the pH range due to its lower standard potential (E^0 (O_2/H_2O) = +1.23 V vs. the standard hydrogen electrode (SHE) and E^0 (Cl_2/Cl^-) = +1.36 V vs. SHE, respectively), CER occurs at a higher rate and has a lower onset potential than OER because of its faster kinetics [8]. Unlike CER, OER is pH-dependent (i.e., E_{OER} decreases with increasing pH). Accordingly, acidic conditions are utilized in the chlor-alkali process to minimize the OER rate and thus its selectivity. In industry, operation at pH $\leq$ 2 is inconvenient because of

the limited stability of the employed membrane materials. Due to the formation of molecular oxygen as a side-product, a significant fraction of the process costs are related to the separation of O_2 from the Cl_2 product stream. Selectivity and stability of the CER and OER anodes have therefore been studied in great detail in the last decades [9–13].

To increase the stability of RuO_2, it is commonly used in a mixture with other oxides such as TiO_2, ZrO_2, and Ta_2O_5 [3,14,15]. This strategy, which results in improved corrosion resistance, was first applied in the fabrication of the so-called dimensionally stable anodes (DSA®), which show enhanced activity and structural stability during operation under corrosive electrochemical conditions [16]. DSAs® are typically composed of a solid solution of rutile TiO_2 and RuO_2 (Ti:Ru atomic ratio ~ 70:30) deposited on a Ti substrate. The mixing of the two components to form a solid solution of the oxides is a key to combine activity and conductivity, provided by RuO_2, with a sufficient stability provided by TiO_2 [17–19]. However, upon prolonged use under harsh industrial CER/OER conditions, even DSAs® suffer from corrosion, which leads to the dissolution of RuO_2. RuO_2 dissolution at anodic potentials can proceed in three ways: (i) oxidation of RuO_2 to volatile RuO_4, (ii) formation of soluble (per)ruthenates and (iii) physical detachment and loss of solid RuO_2 particles [20,21]. The critical anode potential (E_{crit}) is defined as the onset potential of corrosion and is usually ascribed to the oxidation of RuO_2 to RuO_4 (1), which is estimated to occur at about $+1.45\ V_{SHE}$ [22]. It has also been noted by various authors that $E_{crit.}$ matches the onset potential of OER, suggesting that the underlying mechanisms of the two processes are closely related [23–26].

$$RuO_4 + 4H^+ + 4e^- \rightarrow RuO_2 + 2H_2O\ (E^0 = +1.387\ V) \tag{1}$$
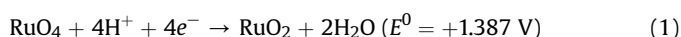
RuO_2 corrosion can occur as transient or steady-state dissolution [15]. The latter is a thermodynamically controlled process and occurs when $E \geq E_{crit}$, while transient dissolution can already occur at much lower overpotential, when low-coordination sites or metastable transition states are exposed to the electrolyte [27]. Transient dissolution was observed for both Ru and RuO_2 electrodes [27,28]. It has also been observed that the lower stability of electrochemically prepared amorphous (hydrous) RuO_2 and the higher stability of thermally prepared crystalline RuO_2 show an inverse relationship with OER activity [27]. This is consistent with the observed correlation of the OER activity and the dissolution rate for a set of transition metals and their oxides [28].

The presence of Cl^- ions has a positive effect on RuO_2 stability. Particularly, RuO_2 and Ru^0 dissolution are slowed down at higher Cl^- concentrations [6]. Since a high concentration of Cl^- is necessary to promote CER over OER, this stabilization can be explained by a lower rate of the OER. However, it has also been shown that an excess of Cl^- in combination with low pH (<2) opens an alternative corrosion route of RuO_2, which is related to the formation of soluble ruthenium chlorides [29].

In the present study, we compare the stability of well-defined $RuO_2(110)/Ru(0001)$ single crystal model anodes under pure OER and competitive CER/OER conditions. The use of model electrodes allows to precise monitoring of structural, morphological and chemical changes of the electrode surface for a selected facet of the active catalyst phase. Besides electrochemical methods, we employed lab- and synchrotron-based characterization techniques, including surface X-ray scattering (SXS) and X-ray reflectivity (XRR), X-ray photoelectron spectroscopy (XPS), inductively-coupled plasma optical emission spectroscopy (ICP-OES), and atomic force microscopy (AFM) to evaluate the degree and type of corrosion occurring during OER and CER treatments. Our multi-technique approach allowed us to follow the structural and compositional changes of the model electrode upon electrochemical treatment in different conditions, enabling a deeper understanding of the nature of the underlying physico-chemical processes involved in anodic corrosion.

2. Experimental section

Preparation of $RuO_2(110)/Ru(0001)$: An ultra-thin $RuO_2(110)$ film was grown epitaxially on sputter-cleaned Ru(0001) single crystals (Surface Preparation Laboratories, Zaandam, NL) with diameters of 7 and 10 mm under ultra-high vacuum (UHV) conditions according to a procedure described elsewhere [30]. In brief, the substrate was cleaned by sequential sputtering/annealing steps until low energy electron diffraction (LEED) showed the pattern characteristic for a clean Ru(0001) surface. Sputtering was carried out at room temperature, $p(Ar) = 1\cdot10^{-6}$ mbar and 600 eV beam energy for a maximum of 15 min in order to prevent crystal damage. Flash annealing was performed by heating the sample with an electron beam heater to 930 °C. The target temperature was maintained for 1 min, after that, the sample was allowed to cool down naturally in the absence of O_2. The cleaning step was followed by a roasting procedure ($p(O_2) = 1\cdot10^{-7}$ mbar, $T = 780$ °C, 20 min) to remove carbon impurities. Then, the growth of $RuO_2(110)$ was carried out at 380 °C for 120 min while $3\cdot10^{-5}$ mbar O_2 were supplied to the preparation chamber via a leak valve. Uniformness of the film and absence of impurities were checked by LEED and XPS, respectively.

Stability evaluation: The electrochemical (EC) stability of $RuO_2(110)/Ru(0001)$ electrodes under O_2 and Cl_2 evolution conditions was evaluated by subjecting the electrodes to continuous potential treatment ($E = +1.50$ V) for 60 min. All potentials reported in this work are plotted versus reversible hydrogen electrode (RHE), if not mentioned otherwise. The potential was chosen to be above the expected critical potential of RuO_2 in order to induce possible electrode degradation, which was assumed to be different under pure OER and competitive OER/CER conditions [6]. The EC treatment was performed in hanging meniscus mode in a standard three-electrode cell filled with 0.5 M H_2SO_4 or 0.5 M HCl (Sigma Aldrich, > 99.99%). Milli-Q (18.2 MΩ cm) water was used in all operations. For simplicity, the experiments conducted in H_2SO_4 and HCl will be further referred to as OER and CER, respectively. Platinum foil (area = 10 cm²) and Red Rod electrodes (Radiometer Analytical, $E_{RE} = +0.215$ V) were utilized as counter (CE) and reference (RE) electrodes, respectively.

The values of the overpotential (η) were calculated using the following equations:

$$\text{for OER: } \eta_{OER} = E_{meas} + E_{Ag/AgCl} + 0.059\ pH - E^0_{OER} \tag{2}$$

$$\text{for CER: } \eta_{CER} = E_{meas} + E_{Ag/AgCl} - E^0_{CER} \tag{3}$$

where E_{meas} is the electrode potential measured against the reference electrode, $E_{Ag/AgCl}$ is the potential of the reference electrode vs. the Standard Hydrogen Electrode (SHE), and E^0 is the standard electrode potentials for the reactions.

Before and after the EC treatment, electrochemical impedance spectroscopy (EIS) measurements were conducted at the open circuit potential in the frequency range of 0.1 Hz–100 kHz with an amplitude of 10 mV. The double-layer capacitances were evaluated from the Nyquist plots by fitting the system with an $R_1(R_2C)$ circuit using Nova Software (version 1.10), where C represents the double-layer capacitance of the samples. The values of the Electrochemical Surface Area (ECSA) were estimated by dividing the values of the double-layer capacitance with the constant value of specific capacitance for ideally flat surfaces in acidic solution (35 μF cm⁻²) [31]. The corresponding roughness factors were then calculated

dividing the values of ECSA with the values of geometric area of the electrodes.

Online electrochemical mass spectrometry (OLEMS): OLEMS measurements were carried out in a three-electrode EC cell in a configuration similar to the one described above. $RuO_2(110)$/Ru(0001) single crystals were mounted into the PEEK sample holder with a bottom contact and used as working electrodes. The holder was additionally covered by several layers of Teflon™ tape (Swagelok) to prevent electrolyte interaction with the contact wire. EC treatment was performed using an Ivium Compactstat potentiostat (Ivium Technologies). OLEMS measurements were conducted with a quadrupole mass spectrometer (Balzers Quadstar, Prisma QME 200) at an operating pressure of approximately $5 \cdot 10^{-7}$ mbar. A more detailed description of the utilized OLEMS setup is given elsewhere [30,32].

In order to evaluate the onset potentials of OER and CER and to derive Faraday plots (see ESI for details), OLEMS measurements were conducted in 0.5 M H_2SO_4 and 0.5 M HCl, respectively.

In the case of 0.5 M H_2SO_4, potential pulses (duration 10 s) were alternated with pulses at the resting potential (t = 90 s, $E = +0.70$ V). Ion currents of $m/z = 32$ (O_2^+) and $m/z = 34$ ($H_2O_2^+$) were continuously recorded throughout the experiment. The resting time was necessary to achieve temporal separation of individual OLEMS peaks. A similar procedure was applied in 0.5 M HCl with a slightly different duration and value of the resting potential ($E = +0.80$ V, 300 s). In CER, a longer resting time was necessary due to an increased tailing time of Cl_2 in the OLEMS system. The presence of HCl^+ and Cl^+ rather than Cl_2^+ signals in the mass spectrometer points to dissociation of Cl_2 and recombination with H^+ from water, the main component in the mass spectrometer vacuum chamber [30].

Surface X-ray scattering: Fresh and EC-treated model electrodes were characterized by surface X-ray scattering (SXS) techniques. Ex-situ SXS measurements were performed at the surface diffraction beamline ID03 of the European Synchrotron Radiation Facility (ESRF, Grenoble, France). In this study, we utilized hard X-ray radiation with an energy of 22 keV ($\lambda = 0.564$ Å) focused to a spot size of 370 μm × 30 μm (horizontal × vertical relative to the plane of the sample surface) at the sample position. The measures were conducted using a reference surface unit cell based on the Ru hcp primitive unit cell, where the h and k vectors are laying parallel to the sample surface and l is normal to the surface and the lattice parameters are: $a = b = 2.706$ Å, $c = 4.282$ Å, $\alpha = \beta = 90°$, $\gamma = 120°$. All the diffraction data reported in this work are referred as the reciprocal space coordinates of such a cell. Structure and crystallinity were evaluated by recording the diffracted intensities along in-plane (h scans) and out of plane crystallographic directions (l scans) at the positions of Ru(0001) and RuO2(110) crystal truncation rods (CTRs). XRR (X-ray reflectivity) measurements were used to evaluate surface roughening. The experiments were conducted using a MAXIPIX [33] installed on the diffractometer arm at a distance of 709 mm from the sample. Visualization, data reduction and fitting of the SXS data were done by the BINoculars script and PyMCA software [32–34]. Measurement errors were determined from the noise level of the separate patterns.

Other characterization methods: XPS measurements of as-prepared samples were carried out on a SPECS XPS spectrometer equipped with a monochromatic small-spot (300 μm) X-ray source, an Al anode (Al $K\alpha = 1486.6$ eV) and a 180° double-focusing hemispherical analyzer with a delay-line detector. The background pressure inside the analysis chamber was kept below 10^{-8} mbar. No additional charge neutralization was applied due to the metallic conductivity of the Ru(0001) substrates. High-resolution and survey spectra were recorded at constant pass energies of 20 eV and 40 eV, respectively. Spectra were calibrated by

setting the binding energy of the Ru^0 ($3d_{5/2}$) component equal to 280.1 eV [34]. XPS spectra were taken at different positions on the surface to average the obtained quantitative results. LEED patterns were recorded with a 4-grid LEED optics (SPECS GmbH) integrated into the UHV preparation chamber of a SPECS NAP-XPS system.

XPS measurements of tested samples were carried out on a K-Alpha XP spectrometer (Thermo Scientific). A different spectrometer was used to allow mapping of the surface with a built-in top-view video microscope. Differences from the previously described XPS machine include spot size (400 μm), number of delay line detector channels (128) and pass energy (50 eV for high-resolution spectra, 200 eV for survey spectra).

Non-contact (tapping mode) atomic force microscopy (AFM) measurements were carried out on an NT-MDT Next microscope. Micrographs were recorded using gold-coated Si probes with a curvature radius of 10 nm (NSG10, NT-MDT). Scanning electron micrographs (SEM) and energy-dispersive X-ray spectra (EDXS) were taken on an FEI Quanta 3D FEG microscope at an accelerating voltage of 15 kV without any additional coating of the surface.

Inductively Coupled Plasma Optical Emission Spectrometry (ICP-OES) measurements were performed on a SPECTROBLUE EOP spectrometer equipped with an axial plasma source (Ar). The sample uptake rate was set to 2 mL/min. The emission intensity of dissolved Ru ions was measured at 240.3 and 267.9 nm.

3. Results and discussion

3.1. Preparation of fresh $RuO_2(110)$/Ru(0001) model electrodes

Single crystal $RuO_2(110)$/Ru(0001) model anodes were prepared by thermal oxidation according to a procedure described elsewhere [30]. Ru(0001) single crystals were repeatedly subjected to a sequence of sputtering/annealing steps followed by a roasting procedure prior to thermal oxidation to RuO_2. The cleanliness of the Ru(0001) single crystals was evaluated by LEED. $RuO_2(110)$ was prepared by thermal oxidation of Ru(0001) at $T = 380$ °C and $p(O_2) = 3 \cdot 10^{-5}$ mbar for 120 min until LEED revealed the disappearance of Ru(0001) reflections and the appearance of three rotational domains characteristic for $RuO_2(110)$ (Fig. 1) [30].
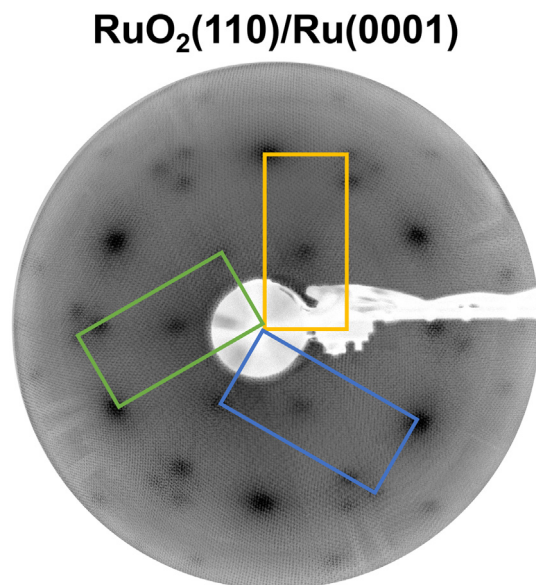
$RuO_2(110)$/Ru(0001)

Fig. 1. LEED pattern of as-prepared $RuO_2(110)$/Ru(0001) taken at 65 eV electron energy. The rectangles display the rotational domains of $RuO_2(110)$.

Then, crystals were UHV-transferred to a SPECS XP spectrometer connected to the preparation chamber and both Ru 3d and survey XP spectra were recorded. Both spectra contain only Ru^0 and RuO_2-related peaks and no additional (in)organic impurities were observed (Fig. 2a and b). The analysis of the Ru 3d spectra (Fig. 2b) shows the presence of three doublets attributable to Ru^0 (BE(Ru $3d_{5/2}$) = 280.1 eV), RuO_2 (BE(Ru $3d_{5/2}$) = 280.7 eV) and RuO_2 shakeups (BE(Ru $3d_{5/2}$) = 282.5 eV) [34]. Based on these three components, the RuO_2 related species amount to 63.4 ± 0.9 at% and 47.7 ± 0.8 at% of the total Ru $3d_{5/2}$ peak area for the two different $RuO_2(110)/Ru(0001)$ samples, respectively. The observed difference in the RuO_2 component areas for the two crystals likely relates to the presence of differently thick $RuO_2(110)$ layers. The first sample was subsequently used for CER and the second for OER experiments. Considering the XPS probing depth of a few nm in the measured range of binding energies (BE), the composition corresponds to surface RuO_2 while some bulk Ru^0 remains visible. The thickness of the thermally grown $RuO_2(110)$ layer is estimated to be similar to reported values [35]. SEM analysis of Ru(0001) surface before and after oxidation shows an absence of any noticeable microscopic (μm scale) defects (Fig. 2c and d).

AF micrographs (Figs. S1a–d) show the presence of agglomerates of flat islands (CER fresh sample) or petals (OER fresh sample). The difference in morphology can be explained by microscopic differences of the initial metal surfaces. However, since the LEED patterns of both oxide samples showed the same crystallographic phase (*i.e.* $RuO_2(110)$) while the reflexes of the Ru(0001) substrate being absent, we assumed to have prepared covering layers of $RuO_2(110)$.

3.2. CER and OER performance of $RuO_2(110)/Ru(0001)$

The performance and selectivity of the $RuO_2(110)/Ru(0001)$ model anodes were evaluated using on-line electrochemical mass spectrometry (OLEMS) in 0.5 M H_2SO_4 and 0.5 M HCl solutions. The results of the OLEMS measurements can be represented as a three-dimensional plot which reports the gas production versus the charge and the applied potential (Fig. S2). The two-dimensional plots of gas production versus charge, the so-called Faraday plots, shown in the main text, are projections of those 3D plots. Each data point belongs to a separate potential applied. Faraday plots can be used for the detection of side-reactions, such as electrode degradation and formation of by-products [36]. In the ideal case of a single reaction on a stable electrode, the amount of detected gaseous product is directly proportional to the passed charge, according to the Faraday law of electrolysis. Assuming a constant gas collection efficiency, a change in the slope of the Faraday plot α can be attributed to the presence of side-reactions which contribute to the measured faradaic charge, resulting in a decrease of the faradaic efficiency (FE) of the main reaction.

In 0.5 M H_2SO_4, where OER is expected to be the dominant reaction, oxygen was first detected at +1.45 V (η = 220 mV) during a positive potential scan (Fig. 3a). The extended data set up to +1.64 V is reported in Fig. S3. Upon further increase of the potential, a proportional increase in O_2 production was observed in line with Faraday's law (Fig. 3b). However, at $E > +1.53$ V, the charge spent in the O_2 production decreased nearly two times, as can be seen from the change of α. This can be attributed to the onset of electrochemical oxidation of RuO_2 to RuO_4 (*1*), which is expected to start at
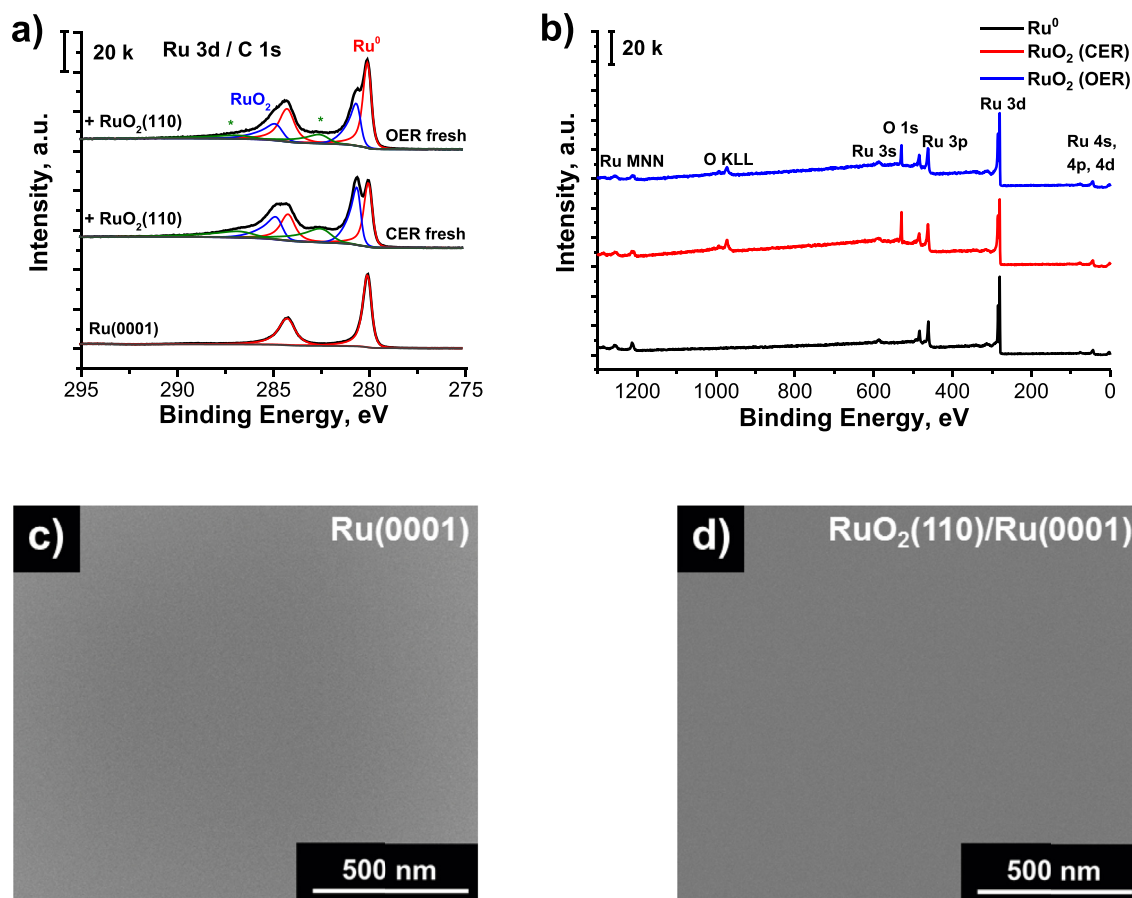

Fig. 2. a) Ru 3d and b) survey XPS spectra of sputter-cleaned Ru(0001) and as-prepared $RuO_2(110)/Ru(0001)$; c, d) corresponding SEM images of the surfaces.
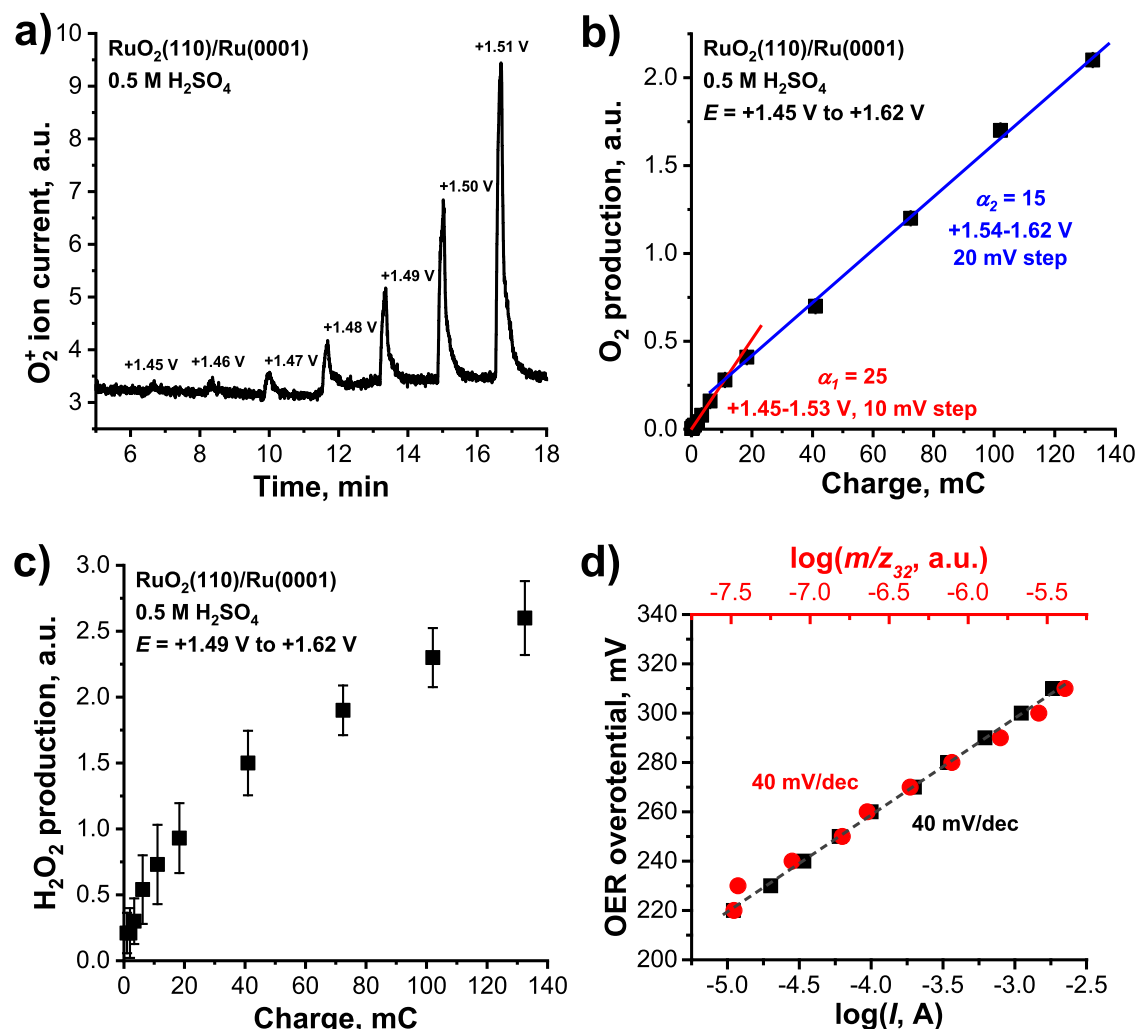
Fig. 3. Potential-dependent ion currents of a) O_2^+ ($m/z = 32$) and corresponding Faraday plots of b) O_2 and c) H_2O_2 evolution; d) Tafel plots derived from voltammograms (black) and $m/z = 32$ (O_2^+) ion current (red) yelding similar Tafel slopes. All plots correspond to $RuO_2(110)/Ru(0001)$ subjected to anodic potential pulses in 0.5 M H_2SO_4. (For interpretation of the references to colour in this figure legend, the reader is referred to the Web version of this article.)

the critical potential [22]. In the studied model system $RuO_2(110)/$ $Ru(0001)$, the metallic substrate will be exposed subsequently, opening new routes of corrosion, as we discuss later in the text. The fact that the OLEMS-measured value of the critical potential is more positive than the values obtained from radiochemical analysis [6] can be explained by the lower sensitivity of OLEMS. To exclude the possibility that H_2O_2 formation contributed to the observed decrease in O_2 production, we monitored its signal (Fig. 3c). H_2O_2 formation was detected by OLEMS at $E \geq +1.49$ V, which is below the observed critical potential [37,38], and its Faraday plot shows a comparable change in the FE as it was observed for O_2. This result indicates that H_2O_2 production was also affected at the critical potential, and hence can be excluded as the main reason for the observed change of Faraday slope.

The OER performance was further evaluated by a Tafel plot analysis (Fig. 3d). The OLEMS-based Tafel plot was constructed from the potential-dependent O_2^+ ($m/z = 32$) ion current [24]. Unlike current density, the OLEMS $m/z = 32$ signal is specific for O_2 only and does not account for products of possible side-reactions, such as RuO_2 oxidation. Tafel slopes of both current- and OLEMS-derived Tafel plots were found to match: the value of 40 mV/dec indicates that a second-electron transfer-process is the rate-determining

step of the OER [39], and no deviations due to surface rearrangement were observed [40]. A value of 40 mV/dec is intermediate between Tafel slopes expected for $RuO_2(110)$ (~60 mV/dec) [39,41] and metallic Ru (30 mV/dec) [20,42], indicating that the exposure of the underneath substrate to the electrolyte took place, as we will discuss further below.

A potential treatment was applied to $RuO_2(110)/Ru(0001)$ in 0.5 M HCl, where Cl_2 evolution is expected to occur along with OER. Indeed, Cl_2 gas was detected for $E \geq +1.44$ V ($\eta_{CER} = 80$ mV), which matches well with the reported values of the CER onset potential for RuO_2 (Fig. 4a) [6,43]. In the presence of Cl^-, O_2 evolution was only observed at $E \geq +1.50$ V ($\eta_{OER} = 270$ mV) which is 50 mV more positive than the OER onset potential in 0.5 M H_2SO_4 (Fig. 4a and c). The origin of this shift has to be found in the competitive adsorption of Cl^- ions on the on-top oxygen species on undercoordinated Ru atom (Ru-O_{ot}), which is regarded as the active surface phase on $RuO_2(110)$ for both the CER and OER [41]. The start of the competition between these two reactions can also be observed in the corresponding Faraday plots of Cl_2 and O_2. In the Cl_2 Faraday plot (Fig. 4b), we can observe a change in the slope similar to the case of O_2 production in 0.5 M H_2SO_4. While the change is located at a similar potential as in the previous experiment, the onset of OER is
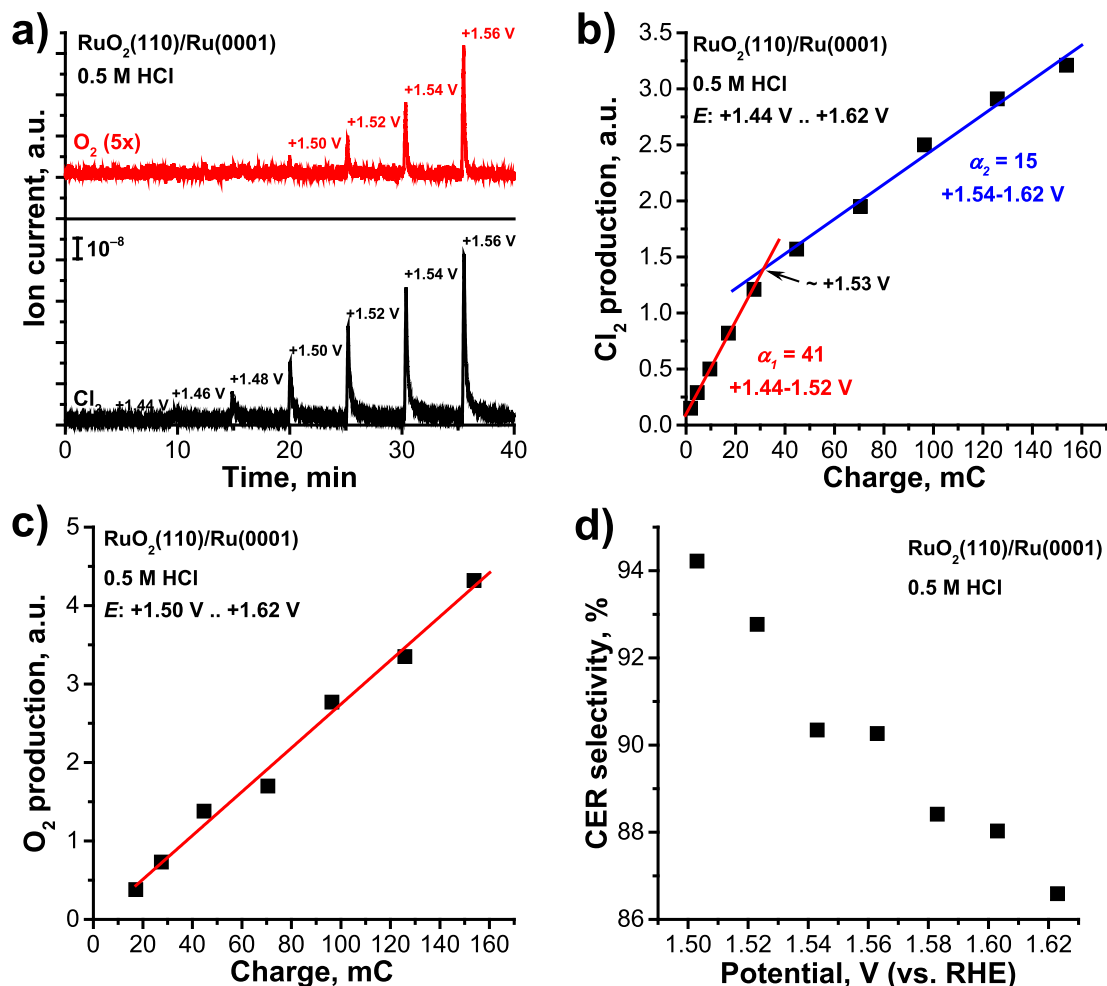
Fig. 4. a) O_2^+ ($m/z = 32$) and $H^{35}Cl^+$ ($m/z = 36$) ion currents and corresponding Faraday plots of potential-dependent b) Cl_2 and c) O_2 evolution under applied anodic pulses recorded on $RuO_2(110)/Ru(0001)$ in 0.5 M HCl; d) estimated selectivity of the CER vs. OER as a function of applied potential.

shifted anodically. This observation indicates that the onset of RuO_2 dissolution is not affected by the OER rate. Unfortunately, we were not able to evidence a change in the O_2 Faraday plot in the 0.5 M HCl experiment, because of the insufficient number of points between the onset of OER and the critical potential, caused by the later onset of OER in this case.

A discrepancy regarding the correlation between the RuO_2 corrosion and OER is present in the literature, where some works found that their onset potentials should necessarily coincide [26,44], while in other more recent papers OER and RuO_2 dissolution were not found to be in tradeoff correlation [27,45,46]. In our experiments, we show that the onset potential of the OER is not necessarily matching this critical potential. For instance, the onset potential of OER can be shifted by increasing selectivity towards CER, while at the same time the critical potential remains independent from the major reaction (Table 1). Thus, we conclude that the critical potential for RuO_2 corrosion and the onset potential of the OER are not linked to each other. Our results support the conclusion of Hodnik et al. [27] that the onsets of OER and of RuO_2 dissolution do not coincide.

Because of the presence of the metallic Ru substrate in our system the corrosion mechanism at higher potentials involves two corrosion routes: the dissolution of RuO_2 and, at the same time, the dissolution of metallic Ru [28]. When metallic Ru gets exposed, the

Table 1
Dependence of the critical potential on OER selectivity and the OER onset potential.

[a]OER selectivity = $\dfrac{\text{OLEMS signal}(O_2)}{\text{OLEMS signal}(O_2) + \text{OLEMS signal}(Cl_2)} \cdot 100\%$.

	0.5 M HCl	0.5 M H$_2$SO$_4$
Onset potential of Cl$_2$ production, V	+1.44	n/a
Onset potential of O$_2$ production, V	+1.50	+1.45
Critical potential, V	+1.53	+1.53
OER selectivity[a] at $E = +1.53$ V, %	< 8	~98

dissolution is accelerated, as reported in previous works [47], because corrosion, in this case, can also take place as a result of direct anodic dissolution of the Ru metal [27].

The potential-dependent CER selectivity (S3) was found to decrease by $5.9 \pm 0.4\%$ per 0.1 V at $E > +1.50$ V (Fig. 4d). It should be noted that, for a more accurate assessment of the electrode selectivity, the actual RuO_2 corrosion rate must be taken into account, which could be achieved by complementary online ICP-MS measurements [15,28,48].

3.3. Stability of RuO$_2$(110)/Ru(0001) under CER and OER

In order to study the stability of the model electrodes with respect to the dominant reaction being either OER or CER, a

potentiostatic treatment was conducted in 0.5 M H_2SO_4 and 0.5 M HCl, respectively. In both cases, the electrodes were mounted in a hanging-meniscus configuration to avoid contact of electrolyte with the sides of the crystals and subjected to a potentiostatic treatment ($E = +1.50$ V) for 60 min (Fig. S4). A variety of different characterization techniques was utilized before and after the electrochemical treatment to evaluate structural, morphological and compositional changes of the model electrode surfaces.

Diffracted intensities along the (10l) rod of RuO_2 films were recorded for the fresh and tested electrodes. From the variation of the intensities of the Bragg reflections of the film along the l direction, it is possible to extract information about the impact of the EC treatment on the out-of-plane domain size of the RuO_2 crystallites composing the $RuO_2(110)$ film (Fig. 5a and Table 2). The FWHM of the relevant reflections was used to determine the out-of-plane crystallite domain size (*i.e.* the thickness of the $RuO_2(110)$ films) via the Scherrer equation (see equation S3). These sizes were determined to be 2.0 ± 0.1 nm and 1.7 ± 0.1 nm for the samples exposed to testing in HCl and H_2SO_4, respectively, and remained nearly unaffected by the EC treatment [35]. The difference in the thickness of the $RuO_2(110)$ layers in the fresh crystals is in line with XPS spectra (Fig. 2a), which pointed at a higher oxide content on the crystal used in the CER experiment. The comparison of the results between fresh and tested samples indicate an overall preservation of the $RuO_2(110)$ thickness upon electrochemical treatment.

XRR experiments allow determining the roughness of the samples independently from their crystallinity. While the intensity along the RuO_2 rod remains largely unchanged upon EC treatment, XRR data presented in Fig. 5b show a slightly increased roughness of the surface, as evident from a steeper decrease of the reflectivity profiles of the spent electrodes accompanied by a decrease of Kiessig fringes [49]. From the minima and maxima position in the XRR plots, the $RuO_2(110)$ layer of the CER sample was found to be slightly thicker than that of the OER sample. Along the same lines, preservation of the $RuO_2(110)$ phase is visible in *hk* maps (Figs. S5 and S6a and b). Taken the SXS and XRR results together, we can conclude that, apart from the expected degradation of $RuO_2(110)$/ Ru(0001) model electrodes under OER and CER conditions, most of the $RuO_2(110)$ layer is stable.

The SE micrographs of the spent electrodes (Fig. 6a−d) reveal the presence of features with an average diameter of 1 μm on the surfaces of the tested electrodes, differently from the surfaces of the samples prior to the electrochemical treatments (Fig. 2c and d). These features appear in the form of pits with a hole in the middle of each individual feature, which are assumed to be the centers of the initial corrosion. The islands are prone to form agglomerates located mostly along with defect sites of the crystal (*e.g.* nanoscratches, centers of mismatch between rotational domains of $RuO_2(110)$) [50]. These features were observed both in HCl and H_2SO_4. However, the area of the surface covered with such islands (R1) was found to be dependent on the performed EC treatment. Particularly, in the case of the OER treatment, 58 ± 3% of the electrode surface was found to be covered with islands, while for CER this was only 16.5 ± 0.6%. EDXS analysis of the chemical composition of both island-covered (R1) and island-free (R2) surfaces points towards higher O content in R1 relative to R2 (Fig. S7a).

For the OER-treated sample, Ru 3d XPS spectra taken at R1 areas show a significantly higher RuO_2 to Ru ratio compared to that of R2. In the case of the OER treatment, an overall increase of the RuO_2-related XPS peak area in contrast to the fresh electrode was found to be 17 ± 4% (R1) and 6 ± 2% (R2). The X-ray spot size of the XPS spectrometer was too large to distinguish between R1 and R2 of the CER-treated sample. Thus, the observed increase of RuO_2 peaks (2.3 ± 0.6%) was attributed to a combination of contributions from R1 and R2. As from the RuO_2 rods we observed a similar thickness of the $RuO_2(110)$ layer, we can conclude that regions R1 correspond to corroded areas where an electrochemically grown, hydrous RuO_2 was formed (Fig. 7). The analysis of the O 1s spectra of the corroded regions reveal an increased area of the hydroxyl-related component in respect of the fresh electrode, indicative of the hydrous nature of the oxide formed upon electrochemical treatment (Figs. S7c and d) [51]. We emphasize that this change is relatively small as most of the signal is arising from intact RuO_2 (110) still present in the corroded regions.

Morphology analysis of the spent electrodes by AFM confirms the presence of holes on both CER- and OER-treated samples. Particularly, loosely distributed pits with a depth variation of 20−120 nm were found on the surface of CER-treated sample (Figs. S8a and c and S9), while OER treatment yields a large number of smaller and shallower pits with an average depth of 6 ± 2 nm (Figs. S8b and d). These pits can be attributed to the centers of corrosion previously observed in the SEM images (Fig. 6a−d).

Elemental analysis of the electrolytes after electrochemical testing by ICP-OES showed that Ru dissolved from the anodes in both HCl and H_2SO_4. Overall Ru dissolution rates were determined
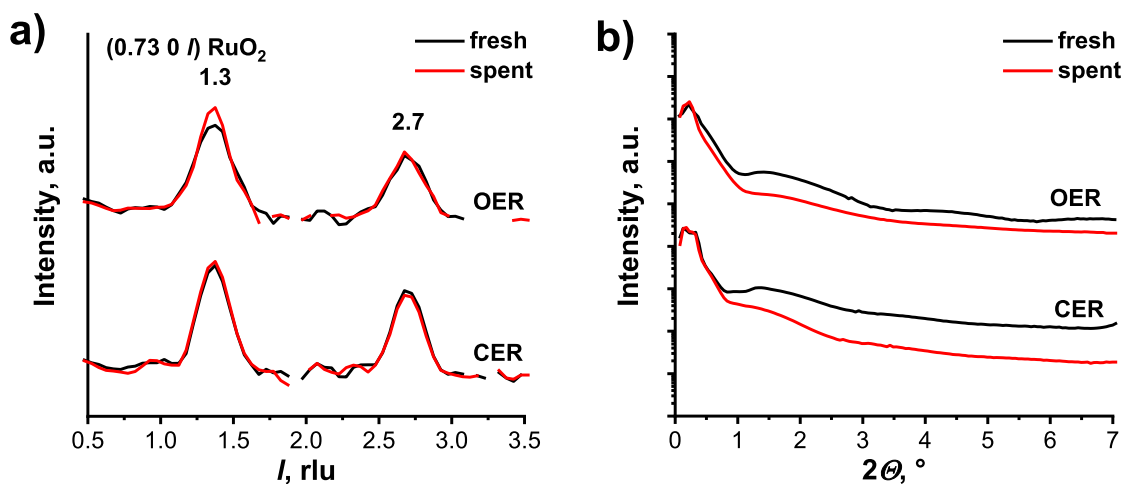

Fig. 5. a) Diffracted intensity of RuO_2 film along the (10l) rod, recorded at (0.73 0 l) respect to the Ru(0001) surface unit cell and b) XRR profiles of fresh and treated $RuO_2(110)$/ Ru(0001) electrodes.

Table 2
RuO$_2$(110) crystallographic changes upon EC treatment.

RuO$_2$(110)	CER (0.5 M HCl)		OER (0.5 M H$_2$SO$_4$)	
	fresh	spent	fresh	spent
[a]Crystallite size (out-of-plane, *l*), nm	2.0 ± 0.1	2.0 ± 0.1	1.7 ± 0.1	1.8 ± 0.1

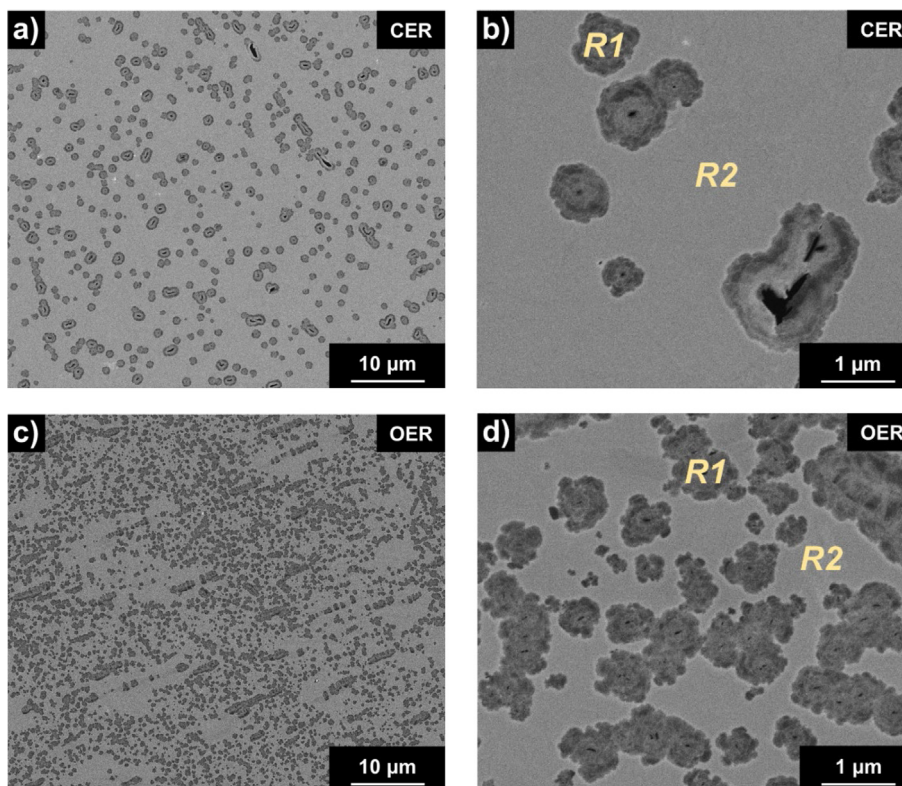[a] Determined from the FWHM of RuO$_2$ (110) peak.

Fig. 6. SE micrographs of RuO$_2$(110)/Ru(0001) electrodes treated at $E = +1.5$ V for 60 min in a-b) 0.5 M HCl, c-d) 0.5 M H$_2$SO$_4$.

and showed that the anode operated in H$_2$SO$_4$ resulted in a much higher dissolution rate (6.27 ± 0.08 μmol h^{-1}·cm^{-2}) compared to the anode operated in HCl (3.01 ± 0.08 μmol h^{-1}·cm^{-2}). This difference in dissolution rates is consistent with values found in the literature [6]. The amount of dissolved Ru detected with ICP-OES after exposing the samples for 1 h at $E = 1.50$ V (1 and 5 μmol in the CER and OER experiments, respectively) is orders of magnitude higher than expected from the dissolution of the RuO$_2$(110) layer only, which would be less than 10 nmol. Thus, it is reasonable to state that the dissolution of bulk Ru(0001) has significantly contributed to the leaching of Ru by pitting corrosion. Moreover, the difference between OER and CER-caused Ru dissolution, measured by ICP-OES, was found to be smaller (2.1 x) than that estimated from the surface coverage of corroded domains (SEM, 3.6 x) (Table 3). The reason for this is that CER led to the formation of fewer but deeper corrosion pits as observed in the AFM profiles.

The pitting corrosion mechanism, which led to the exposure of the underlying, is similar to what has been recently observed in the case of an IrO$_2$(110) layer deposited on RuO$_2$(110/Ru(0001) template under OER conditions [52].

UV−Vis spectra of the spent electrolytes suggest that etched Ru is most likely present in form of Ru(III) chloride aqua complexes with the general formula [RuCl$_n$(H$_2$O)$_{6-n}$]$^{(3-n)+}$ as well as (per)

ruthenates, in the case of CER and OER, respectively (Fig. S10) [26,29,53−55]. Thus, ICP-OES and UV−Vis analyses confirm the electrochemically induced ruthenium leaching at the critical potential, which is likely the reason for the change in the faradaic efficiency of both OER and CER observed by OLEMS.

In order to relate the long-term stability of the model electrodes at the critical potential ($E_{crit.} = +1.50$ V) with their EC activity, a sequence of anodic pulses was applied, while measuring the gas evolution by OLEMS. By combining these data with the results described above, we can correlate the stability of the model RuO$_2$(110)/Ru(0001) anodes with their activity. For both types of acidic electrolytes, similar dependencies were observed (Fig. 8a and b). Firstly, repeated potential pulsing led to an increase of the electrocatalytic activity of the electrode reflected in a current increase. Secondly, both Cl$_2$ and O$_2$ production increased roughly proportionally with the current, in accordance with Faraday's law. The correlation between gas production and total charge points towards constant selectivity of the major reaction at constant potential. From this, we can conclude that the corrosion rate was not changing over time and is only altered by changing the potential. A similar conclusion was drawn for the corrosion of IrO$_2$(110) on RuO$_2$(110)/Ru(0001) in H$_2$SO$_4$ solution [56]. An increase of electrode performance, observed in the form of the proportionally
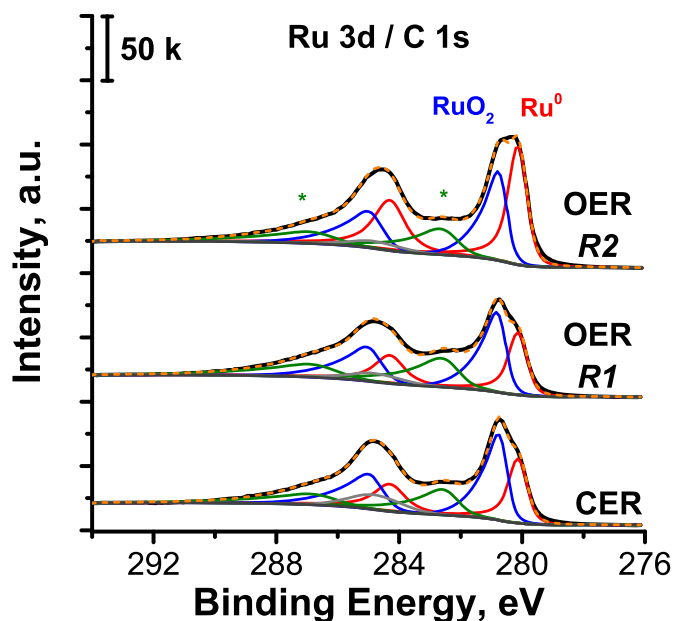
Fig. 7. XPS spectra of combined Ru 3 d/C 1s region of the spent electrodes. Components denoted with * represent the satellite peaks of RuO_2.

Table 3
Estimation of Ru leaching based on ICP-OES and SEM results.

	CER (0.5 M HCl)	OER (0.5 M H$_2$SO$_4$)	Ratio OER/CER
[a]Corroded area (R1, SEM), %	16 ± 1	58 ± 3	3.6
Ru dissolution rate (ICP-OES), $\mu mol \cdot h^{-1} \cdot cm^{-2}$	3.01 ± 0.08	6.27 ± 0.08	2.1

[a] Area covered with corrosion domains (Fig. 6).

increasing current and gas production, can be caused either by an increase of the surface area or by the formation of catalytic sites with higher activity (*e.g.* Ru^0 or electrochemically grown oxide). Higher values of the double-layer capacitance and of the calculated Electrochemical Surface Area (ECSA) were indeed observed in the electrodes after being exposed for 1 h at 1.50 V in 0.5 M HCl and 0.5 M H$_2$SO$_4$ (Table 4). These results can be interpreted as an

Table 4
Values of double-layer capacitance and roughness factors of the samples.

	CER (0.5 M HCl)	OER (0.5 M H$_2$SO$_4$)
Double-layer capacitance, μF	15 (fresh) 92 (tested)	24 (fresh) 334 (tested)
Roughness factor	1.12 (fresh) 6.84 (tested)	0.87 (fresh) 12.15 (tested)

increase of the roughness factor after the electrochemical treatments (particularly in the case of the sample tested in 0.5 M H$_2$SO$_4$), supporting the results of XRR, AFM, and SEM, which highlighted an increased roughness of the spent electrodes.

However, we highlight that the formation of hydrous oxide formed in the pits of corrosion could also contribute to higher the values of the capacitance of the tested samples with its enhanced proton mobility [50]. The increased capacitive current is also reflected in the CVs of the tested samples, especially in the case of H$_2$SO$_4$ electrolyte (Fig. S11). We can neglect the impact of metallic Ru on the observed increase in the catalytic activity since it would rapidly oxidize at $E = +1.50$ V [6,57]. Indeed, no Ru^0 related peaks were observed in the CV scans of the tested electrodes (Figs. S11a and b) [58]. Apart from the larger roughness, the increase in the catalytic activity during time can also be a consequence of the observed formation of electrochemically grown hydrous RuO$_2$, which has been reported to be more active than thermally grown RuO$_2$ [27].

4. Conclusions

RuO$_2$(110)/Ru(0001) single crystal model electrodes were prepared and employed for the evaluation of the stability of RuO$_2$(110) under acidic CER and OER conditions in 0.5 M HCl and 0.5 M H$_2$SO$_4$ electrolytes, respectively. The onset potential of OER is shifted to higher anodic potentials in HCl electrolyte due to the competing CER, while at the same time the critical potential (*i.e.* the onset of RuO$_2$ oxidation) remains independent of the primary electrochemical reaction, indicating that OER and RuO$_2$ dissolution are not coupled.

When electrodes were subjected to the critical potential, a significant dissolution of Ru was observed by elemental analysis of the electrolyte after testing. Pitting corrosion of bulk Ru(0001) can be considered as the main source of dissolved Ru. Despite the
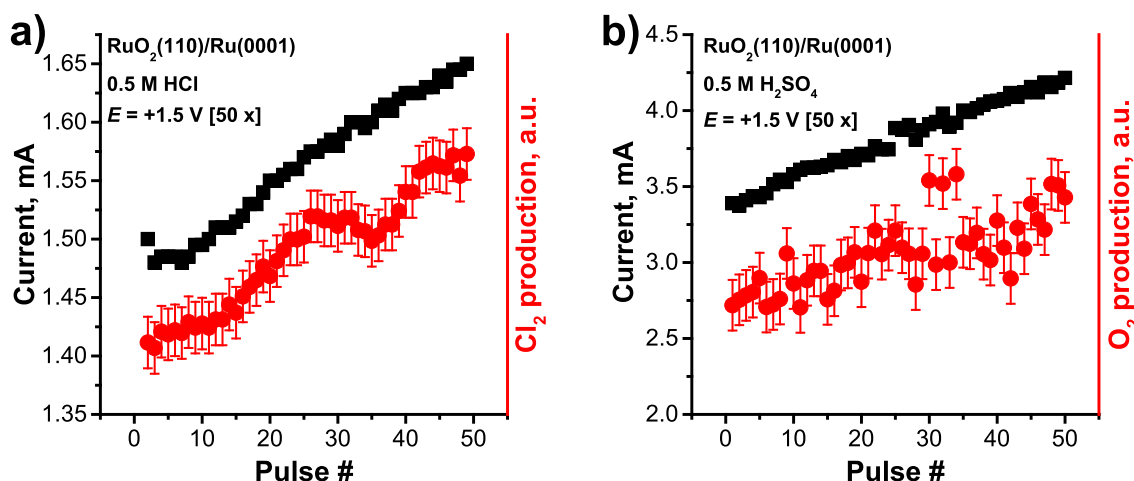

Fig. 8. Electric current and gas production probed under repeated potential pulsing at +1.50 V in a) 0.5 M HCl (product - Cl$_2$) and b) 0.5 M H$_2$SO$_4$ (product - O$_2$).

observed dissolution, electrode corrosion was found to be accompanied by the growth of hydrous RuO_2 due to exposure of the bulk Ru(0001) substrate upon the corrosive treatment. Morphology evaluation of spent electrodes reveals that the corroded areas correspond to the formation of micrometer-sized features (pits), which contain a sub-micrometer pit in the center surrounded by randomly oriented flat petals. The corroded areas revealed significantly higher O content and a higher RuO_2/Ru ratio, indicating an additional growth of electrochemically grown, i.e. hydrous, RuO_2. ICP-OES, SEM, XPS, and EDX analyses all confirmed that the degree of corrosion was higher in the OER case (in H_2SO_4) than in the CER case (in HCl), because the latter reaction reduces the faradaic efficiency of O_2 formation as well as anodic RuO_2 oxidation. The areas not covered with pits showed a similar RuO_2/Ru ratio compared with the fresh samples, indicating that the homogeneous RuO_2(110) layer protects the underlying Ru(0001) from fast corrosion, and its thickness remains to a large extent unchanged after the electrochemical treatment (as seen from the RuO_2 l-scans). The mechanism of RuO_2(110)/Ru(0001) corrosion is proposed to consist of the following steps. Initially, the surface of RuO_2(110) starts dissolving at the critical potential by the formation of anionic Ru compounds in a higher oxidation state, preferably at surface defects (such as points where rotational domains of RuO_2(110) meet). Then, the corrosion of the RuO_2(110) layer causes the exposure of the bulk Ru(0001) substrate, which is more prone to corrosion than the RuO_2(110) surface. Along with the dissolution, the exposed Ru(0001) is oxidized yielding the growth of additional hydrous RuO_2 in the corroded areas. We emphasize that our findings relate to the corrosion behavior of the RuO_2(110) layer on Ru(0001) system, while the corrosion of the underlying metallic substrate is observed as a side reaction and is only related to the nature of the model system. An inert substrate would be necessary to study the mechanism of corrosion of the RuO_2(110) overlayer separately from the underlying substrate.

CRediT authorship contribution statement

Andrey Goryachev: Methodology, Formal analysis, Investigation, Writing - original draft, Visualization. **Marco Etzi Coller Pascuzzi:** Formal analysis, Investigation, Writing - original draft, Visualization. **Francesco Carlà:** Formal analysis, Investigation, Visualization, Writing - review & editing. **Tim Weber:** Formal analysis, Writing - review & editing. **Herbert Over:** Conceptualization, Methodology, Writing - review & editing, Supervision, Funding acquisition. **Emiel J.M. Hensen:** Writing - review & editing, Supervision, Funding acquisition. **Jan P. Hofmann:** Conceptualization, Methodology, Writing - original draft, Writing - review & editing, Supervision, Project administration.

Acknowledgments

Appendix A. Supplementary data

Supplementary data to this article can be found online at https://doi.org/10.1016/j.electacta.2020.135713.

References

[1] S. Trasatti, Electrocatalysis: understanding the success of DSA®, Electrochim. Acta 45 (2000) 2377–2385, https://doi.org/10.1016/S0013-4686(00)00338-8.
[2] H.B. Beer, The invention and industrial development of metal anodes 1, J. Electrochem. Soc. 127 (1980) 303C–307C.
[3] S. Trasatti, Electrocatalysis in the anodic evolution of oxygen and chlorine, Electrochim. Acta 29 (1984) 1503–1512, https://doi.org/10.1016/0013-4686(84)85004-5.
[4] T. Reier, D. Teschner, T. Lunkenbein, Bergmann, S. Selve, R. Kraehnert, R. Schlögl, P. Strasser, Electrocatalytic oxygen evolution on iridium oxide: uncovering catalyst-substrate interactions and active iridium oxide species, J. Electrochem. Soc. 161 (2014) F876–F882, https://doi.org/10.1149/2.0411409jes.
[5] P. Schmittinger, T. Florkiewicz, L.C. Curlin, B. Luke, R. Scannell, T. Navin, E. Zelfel, R. Bartsch, Ullmann's Encyclopedia of Industrial Chemistry, 2012.
[6] R.K.B. Karlsson, A. Cornell, Selectivity between oxygen and chlorine evolution in the chlor-alkali and chlorate processes, Chem. Rev. 116 (2016) 2982–3028, https://doi.org/10.1021/acs.chemrev.5b00389.
[7] J. Fauvarque, The chlorine industry, Pure Appl. Chem. 68 (1996) 1713–1720.
[8] I. Moussallem, J. Jörissen, U. Kunz, S. Pinnow, T. Turek, Chlor-alkali electrolysis with oxygen depolarized cathodes: history, present status and future prospects, J. Appl. Electrochem. 38 (2008) 1177–1194, https://doi.org/10.1007/s10800-008-9556-9.
[9] V. Petrykin, K. Macounova, O.A. Shlyakhtin, P. Krtil, Tailoring the selectivity for electrocatalytic oxygen evolution on ruthenium oxides by zinc substitution, Angew. Chem. Int. Ed. 49 (2010) 4813–4815, https://doi.org/10.1002/anie.200907128.
[10] V. Petrykin, K. MacOunova, J. Franc, O. Shlyakhtin, M. Klementova, S. Mukerjee, P. Krtil, Zn-doped RuO_2 electrocatalyts for selective oxygen evolution: relationship between local structure and electrocatalytic behavior in chloride containing media, Chem. Mater. 23 (2011) 200–207, https://doi.org/10.1021/cm1028782.
[11] A.R. Zeradjanin, N. Menzel, W. Schuhmann, P. Strasser, On the faradaic selectivity and the role of surface inhomogeneity during the chlorine evolution reaction on ternary Ti-Ru-Ir mixed metal oxide electrocatalysts, Phys. Chem. Chem. Phys. 16 (2014) 13741–13747, https://doi.org/10.1039/c4cp00896k.
[12] K. Macounová, M. Makarova, J. Jirkovský, J. Franc, P. Krtil, Parallel oxygen and chlorine evolution on $Ru_{1-x}Ni_xO_{2-y}$ nanostructured electrodes, Electrochim. Acta 53 (2008) 6126–6134, https://doi.org/10.1016/j.electacta.2007.11.014.
[13] V. Petrykin, K. MacOunova, M. Okube, S. Mukerjee, P. Krtil, Local structure of Co doped RuO2 nanocrystalline electrocatalytic materials for chlorine and oxygen evolution, Catal, Today 202 (2013) 63–69, https://doi.org/10.1016/j.cattod.2012.03.075.
[14] C. Comninellis, G.P. Vercesi, Characterization of dsa-type oxygen evolving electrodes. Choice of base metal, J. Appl. Electrochem. 21 (1991) 335–345, https://doi.org/10.1016/0040-6031(91)80257-J.
[15] S. Cherevko, A.R. Zeradjanin, A.A. Topalov, N. Kulyk, I. Katsounaros, K.J.J. Mayrhofer, Dissolution of noble metals during oxygen evolution in acidic media, ChemCatChem 6 (2014) 2219–2223, https://doi.org/10.1002/cctc.201402194.
[16] P. Duby, The history of progress in dimensionally stable anodes, JOM 45 (1993) 41–43, https://doi.org/10.1007/BF03222350.
[17] S. Trasatti, Physical electrochemistry of ceramic oxides, Electrochim. Acta 36 (1991) 225–241, https://doi.org/10.1016/0013-4686(91)85244-2.
[18] F. Hine, M. Yasuda, T. Yoshida, Studies on the oxide-coated metal anodes for chlor-alkali cells, J. Electrochem. Soc. 124 (1977) 500–505, https://doi.org/10.1149/1.2133337.
[19] M. Etzi Coller Pascuzzi, A. Goryachev, J.P. Hofmann, E.J.M. Hensen, Mn promotion of rutile TiO_2-RuO_2 anodes for water oxidation in acidic media, Appl. Catal. B Environ. 261 (2020) 118225, https://doi.org/10.1016/j.apcatb.2019.118225.
[20] C. Iwakura, K. Hirao, H. Tamura, Anodic evolution of oxygen on ruthenium in acidic solutions, Electrochim. Acta 22 (1977) 329–334, https://doi.org/10.1016/0013-4686(77)85082-2.
[21] A.A. Uzbekov, V.G. Lambrev, I.F. Yazikov, N.N. Rodin, L.M. Zabrodskaya, V.S. Klement'eva, Y.M. Vlodov, Corrosion of titanium-supported ruthenium dioxide anodes - nature of anode consumption and ruthenium dissolution kinetics in chloride solutions, Elektrokhimiya 14 (1978) 1150–1159.
[22] I.E. Veselovskaya, S.D. Khodkevich, R.I. Malkina, L.M. Yakimenko, Electro-chemical behavior of ruthenium anode in chlorine and oxygen evolution processe, Elektrokhimiya 10 (1974) 74–77.
[23] R. Kötz, H.J. Lewerenz, S. Stucki, XPS studies of oxygen evolution on Ru and

RuO$_2$ anodes, J. Electrochem. Soc. 130 (1983) 825, https://doi.org/10.1149/1.2119829.

[24] M. Wohlfahrt-Mehrens, J. Heitbaum, Oxygen evolution on Ru and RuO2 electrodes studied using isotope labelling and on-line mass spectrometry, J. Electroanal. Chem. Interfacial Electrochem. 237 (1987) 251−260, https://doi.org/10.1016/0022-0728(87)85237-3.

[25] E. Fabbri, A. Habereder, K. Waltar, R. Kötz, T.J. Schmidt, Developments and perspectives of oxide-based catalysts for the oxygen evolution reaction, Catal. Sci. Technol. 4 (2014) 3800−3821, https://doi.org/10.1039/C4CY00669K.

[26] R. Kötz, S. Stucki, D. Scherson, D.M. Kolb, In-situ identification of RuO4 as the corrosion product during oxygen evolution on ruthenium in acid media, J. Electroanal. Chem. Interfacial Electrochem. 172 (1984) 211−219, https://doi.org/10.1016/0022-0728(84)80187-4.

[27] N. Hodnik, P. Jovanovič, A. Pavlišič, B. Jozinović, M. Zorko, M. Bele, V.S. Šelih, M. Šala, S. Hočevar, M. Gaberšček, New insights into corrosion of ruthenium and ruthenium oxide nanoparticles in acidic media, J. Phys. Chem. C 119 (2015) 10140−10147, https://doi.org/10.1021/acs.jpcc.5b01832.

[28] S. Cherevko, S. Geiger, O. Kasian, N. Kulyk, J.P. Grote, A. Savan, B.R. Shrestha, S. Merzlikin, B. Breitbach, A. Ludwig, K.J.J. Mayrhofer, Oxygen and hydrogen evolution reactions on Ru, RuO2, Ir, and IrO2 thin film electrodes in acidic and alkaline electrolytes: a comparative study on activity and stability, Catal. Today 262 (2016) 170−180, https://doi.org/10.1016/j.cattod.2015.08.014.

[29] T. Loučka, The potential-pH diagram for the Ru−H2O−Cl− system at 25°C, J. Appl. Electrochem. 20 (1990) 522−523, https://doi.org/10.1007/BF01076067.

[30] I. Sohrabnejad-Eskan, A.E. Goryachev, K.S. Exner, L.A. Kibler, E.J.M. Hensen, J.P. Hofmann, H. Over, Temperature-dependent kinetic studies of the chlorine evolution reaction over RuO 2 (110) model electrodes, ACS Catal. 7 (2017) 2403−2411, https://doi.org/10.1021/acscatal.6b03415.

[31] C.C.L. McCrory, S. Jung, J.C. Peters, T.F. Jaramillo, Benchmarking heterogeneous electrocatalysts for the oxygen evolution reaction, J. Am. Chem. Soc. 135 (2013) 16977−16987, https://doi.org/10.1021/ja407115p.

[32] A.H. Wonders, T.H.M. Housmans, V. Rosca, M.T.M. Koper, On-line mass spectrometry system for measurements at single-crystal electrodes in hanging meniscus configuration, J. Appl. Electrochem. 36 (2006) 1215−1221, https://doi.org/10.1007/s10800-006-9173-4.

[33] C. Ponchut, J.M. Rigal, J. Clément, E. Papillon, A. Homs, S. Petitdemange, MAXIPIX, a fast readout photon-counting X-ray area detector for synchrotron applications, J. Instrum. 6 (2011), https://doi.org/10.1088/1748-0221/6/01/C01069. C01069−C01069.

[34] D.J. Morgan, Resolving ruthenium: XPS studies of common ruthenium materials, Surf. Interface Anal. 47 (2015) 1072−1079, https://doi.org/10.1002/sia.5852.

[35] Y.B. He, M. Knapp, E. Lundgren, H. Over, Ru(0001) model catalyst under oxidizing and reducing reaction conditions: in-situ high-pressure surface X-ray diffraction study, J. Phys. Chem. B 109 (2005) 21825−21830, https://doi.org/10.1021/jp0538520.

[36] A. Goryachev, L. Gao, Y. Zhang, R.Y. Rohling, R.H.J. Vervuurt, A.A. Bol, J.P. Hofmann, E.J.M. Hensen, Stability of CoP x electrocatalysts in continuous and interrupted acidic electrolysis of water, ChemElectroChem 5 (2018) 1230−1239, https://doi.org/10.1002/celc.201701119.

[37] R. Gerischer, H. Gerischer, Über die katalytische Zersetzung von Wasserstoffsuperoxyd an metallischem Platin, Z. Phys. Chem. 6 (1956) 178−200, https://doi.org/10.1524/zpch.1956.6.3_4.178.

[38] L.D. Burke, O.J. Murphy, J.F. O'Neill, S. Venkatesan, The oxygen electrode. Part 8.—oxygen evolution at ruthenium dioxide anodes, J. Chem. Soc. Faraday Trans. 1 Phys. Chem. Condens. Phases. 73 (1977) 1659, https://doi.org/10.1039/f19777301659.

[39] Y.H. Fang, Z.P. Liu, Mechanism and tafel lines of electro-oxidation of water to oxygen on RuO2(110), J. Am. Chem. Soc. 132 (2010) 18214−18222, https://doi.org/10.1021/ja1069272.

[40] P. Castelli, S. Trasatti, Single crystals as model electrocatalysts, J. Electroanal. Chem. 210 (1986) 189−194.

[41] K.S. Exner, I. Sohrabnejad-Eskan, H. Over, A universal approach to determine the free energy diagram of an electrocatalytic reaction, ACS Catal. 8 (2018) 1864−1879, https://doi.org/10.1021/acscatal.7b03142.

[42] H. Tamura, C. Iwakura, Metal oxide anodes for oxygen evolution, Int. J. Hydrogen Energy 7 (1982) 857−865, https://doi.org/10.1016/0360-3199(82)90003-9.

[43] T. Arikawa, Y. Murakami, Y. Takasu, Simultaneous determination of chlorine and oxygen evolving at RuO2/Ti and RuO2-TiO2/Ti anodes by differential electrochemical mass spectrometry, J. Appl. Electrochem. 28 (1998) 511−516, https://doi.org/10.1023/a:1003269228566.

[44] R. Kotz, H.J. Lewerenz, S. Stucki, XPS studies onf oxygen evolution on Ru and RuO2 anodes, J. Electrochem. Soc. 130 (1983) 825−829.

[45] N. Danilovic, R. Subbaraman, K.C. Chang, S.H. Chang, Y. Kang, J. Snyder, A.P. Paulikas, D. Strmcnik, Y.T. Kim, D. Myers, V.R. Stamenkovic, N.M. Markovic, Using surface segregation to design stable Ru-Ir oxides for the oxygen evolution reaction in acidic environments, Angew. Chem. Int. Ed. 53 (2014) 14016−14021, https://doi.org/10.1002/anie.201406455.

[46] A.R. Zeradjanin, A.A. Topalov, Q. Van Overmeere, S. Cherevko, X. Chen, E. Ventosa, W. Schuhmann, K.J.J. Mayrhofer, Rational design of the electrode morphology for oxygen evolution − enhancing the performance for catalytic water oxidation, RSC Adv. 4 (2014) 9579, https://doi.org/10.1039/c3ra45998e.

[47] N. Danilovic, R. Subbaraman, K.C. Chang, S.H. Chang, Y.J. Kang, J. Snyder, A.P. Paulikas, D. Strmcnik, Y.T. Kim, D. Myers, V.R. Stamenkovic, N.M. Markovic, Activity-stability trends for the oxygen evolution reaction on monometallic oxides in acidic environments, J. Phys. Chem. Lett. 5 (2014) 2474−2478, https://doi.org/10.1021/jz501061n.

[48] S. Cherevko, Electrochemical dissolution of noble metals native oxides, J. Electroanal. Chem. 787 (2017) 11−13, https://doi.org/10.1016/j.jelechem.2017.01.029.

[49] E. Chason, T.M. Mayer, Thin film and surface characterization by specular X-ray reflectivity, Crit. Rev. Solid State Mater. Sci. 22 (1997) 1−67, https://doi.org/10.1080/10408439708241258.

[50] H. Over, Surface chemistry of ruthenium dioxide in heterogeneous Catalysis and electrocatalysis: from fundamental to applied Research, Chem. Rev. 112 (2012) 3356−3426, https://doi.org/10.1021/cr200247n.

[51] P.P.T. Krause, H. Camuka, T. Leichtweiss, H. Over, Temperature-induced transformation of electrochemically formed hydrous RuO$_2$ layers over Ru(0001) model electrodes, Nanoscale 8 (2016) 13944−13953, https://doi.org/10.1039/c6nr00732e.

[52] T. Weber, J. Pfrommer, M.J.S. Abb, B. Herd, O. Khalid, M. Rohnke, P.H. Lakner, J. Evertsson, S. Volkov, F. Bertram, R. Znaiguia, F. Carla, V. Vonk, E. Lundgren, A. Stierle, H. Over, Potential-induced pitting corrosion of an IrO$_2$(110)-RuO$_2$(110)/Ru(0001) model electrode under oxygen evolution reaction conditions, ACS Catal. 9 (2019) 6530−6539, https://doi.org/10.1021/acscatal.9b01402.

[53] J.-Y. Chen, Y.-C. Hsieh, L.-Y. Wang, P.-W. Wu, Electroless deposition of Ru films via an oxidative-reductive mechanism, J. Electrochem. Soc. 158 (2011) D463, https://doi.org/10.1149/1.3592996.

[54] E.E. Mercer, W.A. McAllister, The Dipole Moments ofcis- andtrans-Tri-chlorotriaquoruthenium(III), Inorg. Chem. 4 (1965) 1414−1416, https://doi.org/10.1021/ic50032a009.

[55] R.E. Connick, C.R. Hurley, Chemistry of Ru(VI), -(VII) and -(VIII). Reactions, oxidation potentials and spectra, J. Am. Chem. Soc. 74 (1952) 5012−5015, https://doi.org/10.1021/ja01140a007.

[56] T. Weber, T. Ortmann, D. Escalera-López, M.J.S. Abb, B. Mogwitz, S. Cherevko, M. Rohnke, H. Over, Visualizing potential-induced pitting corrosion of ultra-thin single-crystalline IrO$_2$(110) films on RuO$_2$(110)/Ru(0001) under electrochemical water splitting conditions, ChemCatChem 11 (2019) 1−13, https://doi.org/10.1002/cctc.201901674.

[57] M. Pourbaix, Atlas of Electrochemical Equilibria in Aqueous Solutions, Pergamon Press, Oxford, New York, 1966.

[58] S. Hadzi-Jordanov, H. Angerstein-Kozlowska, M. Vuković, B.E. Conway, The state of electrodeposited hydrogen at ruthenium electrodes, J. Phys. Chem. 81 (1977) 2271−2279, https://doi.org/10.1021/j100539a016.